PCCP

ROYAL SOCIETY OF CHEMISTRY

PAPER

View Article Online
View Journal | View Issue

Cite this: *Phys. Chem. Chem. Phys.*, 2024, **26**, 14194

Constructing hollow core–shell Z-scheme heterojunction CdS@$CoTiO_3$ nanorods for enhancing the photocatalytic degradation of 2,4-DCP and TC

Jianhua Zheng, *[abc] Yiming Gao,[a] Bingbing Wang,[a] Zhenping Guan,[d] Guangming Yin,*[a] Heshan Zheng,[a] Yong Li,[b] Xiangyu Cao[b] and Shunji Zheng[b]

Constructing Z-scheme heterojunctions incorporating an exquisite hollow structure is an effective performance regulation strategy for the realization of high quantum efficiency and a strong redox ability over photocatalysts. Herein, we report the delicate design and preparation of a core–shell hollow CdS@$CoTiO_3$ Z-scheme heterojunction with a CdS nanoparticle (NP)-constructed outer shell supported on a $CoTiO_3$ nanorod (NR) inner shell. The *in situ* growth synthetic method led to a tightly connected interface for the heterojunction between CdS and $CoTiO_3$, which shortened the transport distance of photoinduced charges from the interface to the surface. The promoted charge carrier separation efficiency and the retained strong redox capacity caused by the Z-scheme photoinduced charge-transfer mechanism were mainly responsible for the boosted photocatalytic performance. Additionally, the well-designed core–shell structure afforded a larger interfacial area by the multiple direction contact between CdS and $CoTiO_3$, ensuring sufficient channels for efficient charge transfer, and thus further boosting the photocatalytic activity. As an efficient photocatalyst, the optimized CdS@$CoTiO_3$ nanohybrids displayed excellent 2,4-dichlorophenol (2,4-DCP) and tetracycline (TC) degradation efficiencies of 91.3% and 91.8%, respectively. This study presents a Z-scheme heterojunction based on ecofriendly $CoTiO_3$, which could be valuable for the development of metal perovskite photocatalysts for application in environmental remediation, and also demonstrated the tremendous potential of integrating a Z-scheme heterojunction with the morphology design of photocatalyts.

Received 26th March 2024,
Accepted 23rd April 2024

DOI: 10.1039/d4cp01266f

rsc.li/pccp

1. Introduction

The photocatalytic remediation of waste effluent containing toxic organic pollutants is a promising strategy to mitigate the ever-increasing environmental pollution crisis owing to its satisfactory catalytic efficiency and ecofriendly features. However, the practical application of photocatalysis is still limited due to most current photocatalyts suffering from poor visible-light-absorption performance and a fast recombination of photoinduced carriers.[1–3] Developing efficient photocatalyts is highly desirable to promote the practical implementation of photocatalysis. Rationally constructing a heterojunction is an effective strategy to accelerate the spatial separation of photoinduced carriers in semiconductors and the supply of more potential catalytic sites compared to in the single-component counterparts.[4,5] In particular, by forming a Z-scheme heterojunction, a wide light-absorption range and sufficient redox capacity can be simultaneously achieved, ascribed to the Z-scheme charge-transfer path with the assistance of the built-in electric field in the heterojunction region, which can thus enhance the photocatalytic performance.[6–9] Recently, a number of Z-scheme heterojunctions such as g-C_3N_4/MoS_2,[10] $CdIn_2S_4$/ZnS,[11] CoS*x*/CdS,[12] and BiOCl/Bi_2S_3[13] have been constructed with the aim of achieving excellent photocatalytic performances. Additionally, assembling low-dimensional nanoscale building blocks to form hierarchical hollow configurations is reported as another commendable method for improving the photocatalytic performance.[14,15] This is mainly because hierarchical hollow structures possess multiple intrinsic advantages, including improved light absorption, expedited photoinduced carrier separation and migration, and enhanced surface redox reactions.[16–20] So far, numerous nanomaterials

[a] College of Chemistry and Chemical Engineering, Qiqihar University, Qiqihar, Heilongjiang 161006, China
[b] College of Light Industry and Textiles, Qiqihar University, Qiqihar, Heilongjiang 161006, China
[c] Engineering Research Center of Flax Processing Technology (Qiqihar University), Ministry of Education, Qiqihar, Heilongjiang 161006, P. R. China
[d] College of Mechanical and Electrical Engineering, Qiqihar University, Qiqihar 161000, China

with hierarchical hollow configurations have been developed as photocatalysts to catalyze CO_2 conversion,[21] water splitting reactions,[22] and the photocatalytic degradation of pollutants.[23] Z-scheme heterojunction photocatalysts can further accelerate the separation and direct transfer of light-induced electron–hole pairs to promote the redox reactions. It is noteworthy that forming core–shell structures with distinct boundaries can not only provide larger active interfaces between the constituent materials by multiple directional contact, but also produce new synergetic effects owing to the ranges of physical and chemical properties of the core and shell influenced by their compositions, structures, and dimensions, making them attractive for applications in catalysis.[24,25] For example, Zhu *et al.*[26] prepared a Sn^{2+}-ion self-doping CdS/$ZnSnO_3$ hollow core–shell cubic heterojunction photocatalyst, which demonstrated significantly improved photocatalytic activity for the hydrogen evolution reaction and for ciprofloxacin degradation under visible-light irradiation.

Among the numerous reported photocatalysts, perovskite oxide $CoTiO_3$ has aroused much interest recently owing to its superior photoelectronic properties, visible-light-responsive band gap ($E_g \approx 2.3$), and high carrier mobility. In particular, its unique ABO_3 structure can increase ionic defects or oxygen vacancies *via* holding more cations, resulting in improved photocatalytic performances.[27,28] Importantly, $CoTiO_3$ possess a high valence band potential ($E_v \approx 2.3$) that endow E_v holes with strong oxidizability. $CoTiO_3$-based photocatalytic materials have already been exploited for pollutant degradation and have achieved excellent performances.[29–31] Apparently, the introduction of a complementary semiconductor with a strong reduction capacity to construct Z-scheme heterojunctions with $CoTiO_3$ can not only contribute to promoting a strong redox ability but also fast carrier separation and transportation, thus further improving the photocatalytic performance. CdS with a moderate band gap ($\approx$2.4 eV) has been widely reported to be a remarkable photocatalyst.[32–34] Moreover, CdS possessing the required conduction band potential (E_C) of about −0.5 V is more negative than that of $CoTiO_3$, which makes it one of the potential candidates to construct Z-scheme heterojunctions with $CoTiO_3$. The fabrication of heterostructured nanocomposites of $CoTiO_3$ by combining with CdS can not only endow the hybrids with novel characteristics, but also improve their efficiency due to synergistic effects. The given background supports the feasibility of synergistic photocatalysis by combining $CoTiO_3$ and CdS. Yet, to the best of our knowledge, the use of hybrids of CdS and $CoTiO_3$ as an efficient photocatalyst for the degradation of toxic organic pollutants in waste effluents has not been reported previously.

To realize the ingenious synergistic advantages of a Z-scheme heterojunction and a hollow structure, a hierarchical hollow CdS@$CoTiO_3$ Z-scheme heterojunction was obtained by the *in situ* growth of CdS NPs on the surface of $CoTiO_3$ NRs, in which the $CoTiO_3$ NRs served as an outstanding matrix that could also greatly prevent the CdS NPs from agglomerating. The unique structure promoted the separation and transfer of photogenerated charges, while also offering a large surface area for target pollutants adsorption, and the exposure of abundant active sites for surface catalysis. Accordingly, the optimized CdS@$CoTiO_3$ hybrids manifested superior activity for the visible-light degradation of 2,4-DCP and TC, achieving remarkable degradation efficiencies of ~91.3% (2,4-DCP) and 91.8% (TC), respectively. Additionally, CdS@$CoTiO_3$ exhibited remarkable stability over four successive cycles of the degradation process. Based on the experiment results, the enhanced photocatalytic degradation mechanism of CdS@$CoTiO_3$ is proposed.

2. Experimental section

2.1. Materials

The key reagents were $Co(CH_3COOH)_2{\cdot}4H_2O$, tetrabutyl titanate, ethylene glycol (EG), diethylenetriamine (DETA), $CdSO_4{\cdot}8H_2O$, thiourea, (Kemiou Chemical Reagent Co. Ltd, Tianjin, China), 2,4-dichlorophenol, and tetracycline (Aladdin Biological Co., Ltd, Shanghai, China). All the reagents were of analytical grade.

2.2. Synthesis

2.2.1. Preparation of hollow $CoTiO_3$ nanorods. The $CoTiO_3$ was prepared according to a literature method[35,36] with some modifications as follows: $Co(CH_3COOH)_2{\cdot}4H_2O$ (0.244 g) and butyl titanate (0.4 mL) were mixed with ethylene glycol (60 mL) and vigorously stirred at room temperature for 24 h to obtain light-green Co–Ti–ethylene glycol (Co–Ti–EG–). The Co–Ti–EG– was collected by centrifugation. After washing with ethanol

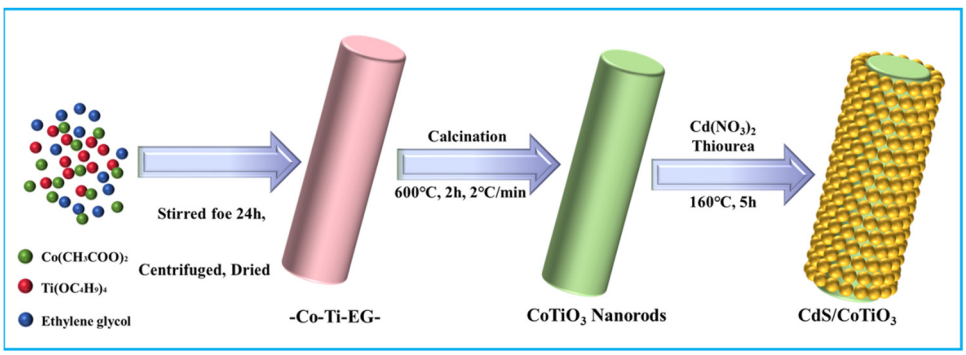

Scheme 1 Illustration of the synthesis of the CdS@$CoTiO_3$ Z- scheme heterojunction.

three times, the obtained Co–Ti–EG– was dried in an oven at 80 °C and calcined at 600 °C for 2 h under vacuum conditions at a heating rate of 2 °C min^{-1} to obtain the $CoTiO_3$ nanorod structures as a green powder.

2.2.2. Preparation of the core–shell CdS@$CoTiO_3$ hybrids. The CdS@$CoTiO_3$ hybrid was synthesized by the *in situ* growth of CdS on the surface of $CoTiO_3$ *via* a facile solvothermal method, as illustrated in Scheme 1. Here, 10%CdS@$CoTiO_3$, 0.0865 g $Cd(NO_3)_2{\cdot}4H_2O$, and 0.0215 g thiourea were added into an 80 mL mixed solvent of 64 mL deionized H_2O and 16 mL DETA, and then a certain amount of $CoTiO_3$ (0.3724 g) was added as the substrate, with stirring for 5 min. After that, the above mixture was transferred to a 100 mL Teflon-lined stainless steel autoclave and kept at 160 °C for 5 h. Finally, the product was washed with water and ethanol three times, collected, and dried in an oven at 80 °C for 24 h. The obtained samples were denoted as *x*CdS@$CoTiO_3$ (where *x* means the mass ratio (%) of CdS relative to $CoTiO_3$, and *x* = 5, 10, 15, and 20). For comparison, pure CdS was prepared by the same method in the absence of $CoTiO_3$.

2.2.3. Characterizations. The morphologies and microstructures of the catalysts were analyzed by SEM (S4800, Hitachi Co., Japan), HRTEM coupled with EDX elemental scanning spectroscopy (S4800, Hitachi Co., Japan and 2100F, JEOL Co. Japan), XRD with Cu Ka radiation (D/max-2200, Rigaku., Japan), and XPS (Thermo Electron, ESCALAB 250 Xi., USA). The UV-visible diffuse reflectance spectra and photoluminescence spectra were acquired using UV2550 and FLS-920T fluorescence spectrophotometers, respectively. The ESR signals were recorded using a Bruker A300 spectrometer. The photoelectrochemical and electrochemical impedance spectra were obtained on a CHI660D electrochemical workstation (Shanghai Chenhua, China).

2.2.4. Evaluation of the photocatalytic degradation activity. Here, 2,4-DCP (10 mg L^{-1}) and TC (10 mg L^{-1}) were selected to estimate the photocatalytic activities of the obtained materials under visible-light irradiation. A 500 W Xenon lamp with a 420 nm cutoff filter (100 mW cm^{-2} light intensity) was used as the visible-light source and the mixture was maintained at around 20 cm distance from it. First, 30 mg photocatalyst was added into a photocatalytic reactor containing 50 mL 2,4-DCP/TC solution and then placed in darkness under magnetic stirring for 40 min at 300 rpm to achieve adsorption–desorption equilibrium. After that, the light source was turned on and 2 mL aqueous was withdrawn from the reactor at certain time intervals, and centrifuged to remove the catalysts. The concentration of 2,4-DCP was monitored using an Agilent 1290 Infinity II ultraperformance liquid chromatography (UPLC) system equipped with a C18 column and UV detector (λ = 284 nm) and the mobile phase was HCOOH and CH_3OH (50/50, *v*:*v*) with a flow rate of 1.0 mL min^{-1}, while TC was analyzed using a Lambda 750S UV/VIS/NIR spectrometer at λ = 358 nm.

The degradation ratio (*R*) of 2,4-DCP and TC was calculated according to the following equation:

$$R\% = \frac{C_0 - C_t}{C_0} \times 100\% \quad (1)$$

where C_0 and C_t denote the 2,4-DCP and TC concentrations in mg L^{-1} at the initial time and at time *t* (min), respectively.

3. Results and discussion

It could be clearly observed that pristine $CoTiO_3$ displayed a rod-like morphology with a length and width of approximately 2 μm and 400 nm, respectively (Fig. 1a), and a definite interior cavity could also be observed (see the inset of Fig. 1a). Meanwhile, the morphology analysis of pure CdS showed it was composed of a great many irregular nanoparticles agglomerated together (Fig. 1b). Following the hydrothermal reaction at 160 °C, CdS NPs uniformly grew on the whole surface of the $CoTiO_3$ NRs to form the shell layer without any agglomeration (Fig. 1c), meaning there was a large contact area between CdS and $CoTiO_3$ to form more heterojunctions. A typical TEM image of the as-derived sample further confirmed the hollow core–shell structure with a thickness of CdS shell layer of about 40 nm, revealing that the incorporation of CdS had no obvious influence on the morphology.

Additionally, HRTEM images for the CdS@$CoTiO_3$ heterojunction are shown in Fig. 2a and b. According to the partially magnified image, a clear heterojunction interface with the intersection of the lattice fringes could be observed, further confirming the forming of the CdS@$CoTiO_3$ heterojunction. The tight anchoring of CdS NPs on the $CoTiO_3$ nanorods favored the formation of intimate interfacial contacts, which is highly beneficial for efficient charge separation/transfer in hybrids.[37] The clear lattice fringe with a spacing of 0.37 nm were attributed to the (012) plane of $CoTiO_3$ nanorods (Fig. 2c), while that of 0.34 nm was assigned to the (002) plane of CdS (Fig. 2d).[38,39] To further obtain information on the elemental composition and distribution for the CdS@$CoTiO_3$ heterojunction photocatalyst, scanning TEM-energy-dispersive X-ray (STEM-EDX) characterization was conducted. As shown in Fig. 2e, it could be observed that the CdS@$CoTiO_3$ heterojunction contained Co, Ti, O, Cd, and S elements, and their distribution was homogeneous, supporting the results obtained from the TEM and HRTEM

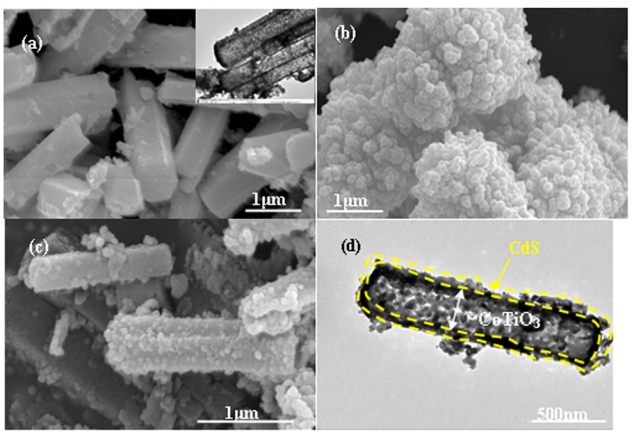

Fig. 1 SEM images: $CoTiO_3$ (inset is the TEM image) (a), CdS (b), CdS@$CoTiO_3$ (c); and TEM image of CdS@$CoTiO_3$ (d).

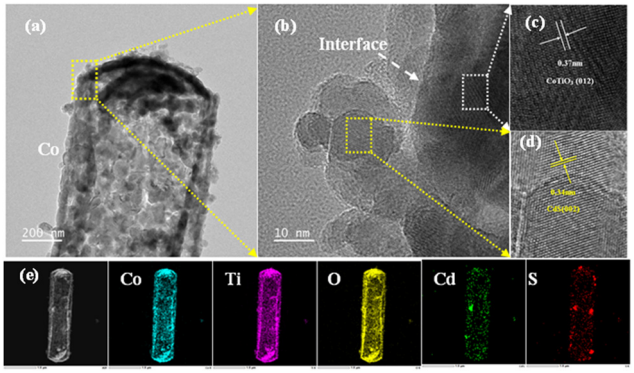

Fig. 2 (a)–(d) HRTEM micrographs and (e) corresponding EDS elemental mapping images of the CdS@$CoTiO_3$ heterojunction.

studies showing that the CdS nanoparticles were uniformly covered on the $CoTiO_3$ core nanostructures.

XPS was performed to obtain information on the elements present and on the alteration in the electronic environments of the different samples. The XPS spectra of $CoTiO_3$, CdS, and CdS@$CoTiO_3$ verified the existence of the corresponding elements (Fig. 3a and b). Fig. 3c illustrates the fine spectra of Co in $CoTiO_3$ and CdS@$CoTiO_3$. The two peaks at about 796.18 and 780.18 eV with their distinguishable satellite peaks (at about 802.38 and 785.68 eV, denoted as Sta.) were indexed to Co 2p3/2 and Co 2p1/2. Moreover, the splitting energy between the Co 2p1/2 and Co 2p3/2 peaks of $CoTiO_3$ and CdS@$CoTiO_3$ were consistent with the theoretical value of 16 eV for Co(II), revealing the presence of Co^{2+} in $CoTiO_3$.[27,40] Notably, the binding energies were positively shifted by 0.60 eV for the CdS@$CoTiO_3$ heterojunction. The Ti 2p spectra for $CoTiO_3$ and CdS@$CoTiO_3$ are portrayed in Fig. 3d, where the peaks at about 457.51 and 463.24 eV were from the 2p3/2 and 2p1/2 orbitals of Ti, respectively.[41,42] After incorporating CdS NPs, the binding energy was 0.57 eV higher than that of pure $CoTiO_3$. The high-resolution O1s XPS spectrum of the CdS@$CoTiO_3$ heterojunction was divided into three peaks, in which the peak at 532.98 eV originated from the –OH groups adsorbed on the surface (Fig. 3e),[43] while the peaks at 530.47 and 529.16 eV represent the oxygen present in the lattice of $CoTiO_3$.[44,45] A positive shift by around 0.20 eV was also observed in the CdS@$CoTiO_3$ heterojunction. At the same time, the binding energies for Cd 3d and S 2p for the CdS@$CoTiO_3$ heterojunction were negatively shifted of 0.20 and 0.50 eV with respect to the pristine CdS NPs, respectively (Fig. 3f and g). It is well accepted that the binding energy is negatively correlated with surface electron density.[46] The positive shifts of the Co 2p, Ti 2p, and O 1s XPS peaks as well as the negative shifts of the Cd 3d and S 2p regions on CdS@$CoTiO_3$ suggested that the electrons transfer from $CoTiO_3$ to CdS, further manifesting that hybrids with efficient electron-transfer processes were formed in the CdS@$CoTiO_3$ heterojunction.[47–49]

Fig. 3h presents the X-ray diffraction (XRD) patterns for CdS, $CoTiO_3$, and a series of CdS@$CoTiO_3$ heterojunctions. For CdS and $CoTiO_3$, all the diffraction peaks matched the respective standard cards (CdS, PDF#10-0454)[50] and ($CoTiO_3$, PDF#15-0866).[51] As for the CdS@$CoTiO_3$ heterojunctions, not only were diffraction peaks corresponding to $CoTiO_3$ observed, but also peaks for CdS. Interestingly, the intensity of the peaks for CdS gradually increased with the dosage increase, which unambiguously confirmed the successful synthesis of the CdS@$CoTiO_3$ heterojunction.

The light-absorption property was investigated by the UV-vis-DRS technique for better exploring the photocatalytic mechanism of the CdS@$CoTiO_3$ hybrids. As shown in Fig. 4a, the absorption edge of the CdS NPs was about 550 nm, concurring with related reports.[13] The pure $CoTiO_3$ NRs displayed optical adsorption properties both in the UV and visible-light regions. Furthermore, absorption peaks centered at about 538 and 605 nm were observed, which could be indexed to metal-to-metal charge transfer (Co^{2+} to Ti $^{4+}$).[52] Notably, after assembling CdS NPs on the $CoTiO_3$ hollow NRs, a stronger absorption intensity was discovered compared to $CoTiO_3$, implying that the CdS@$CoTiO_3$ hybrid enabled efficient light harvesting, which was mainly due to the well-designed core–shell structure, wherein the tightly connected interface accelerated the transmission rate of charge carriers, and thus promoted the photocatalytic performance. According to the transformed Kubelka–Munk function,[53] the corresponding bandgaps of CdS, $CoTiO_3$, and CdS@$CoTiO_3$ were estimated to be 2.23, 2.48, and 2.42, respectively (Fig. 4b).

Subsequently, the band structures of $CoTiO_3$ and CdS were calculated using the following equations:[54,55]

$$E_C = \chi - E_0 - 1/2E_g \quad (2)$$

$$E_V = E_g + E_C \quad (3)$$

where χ and E_g are the bulk electronegativity and bandgap of the semiconductors, respectively, and E_0 represents the energy of free electrons *versus* NHE ($\approx$ 4.5 eV). The estimated values of χ for $CoTiO_3$ and CdS were 5.76 and 5.19 eV, respectively. Hence, E_C and E_V for $CoTiO_3$ were calculated to be 0.02 and 2.50 eV, respectively, while these of CdS were estimated to be −0.43 and 1.80 eV, respectively.

Various photoelectrochemical techniques were applied to obtain insights into the separation and transfer performance of the carriers between CdS and $CoTiO_3$ in the CdS@$CoTiO_3$ hybrid. Compared to CdS and $CoTiO_3$ alone, CdS@$CoTiO_3$ clearly displayed an enhancement in photoelectric current density (Fig. 5a), implying the lowest recombination rate of photogenerated carriers.[56] Moreover, the lower charge-transfer resistance in the CdS@$CoTiO_3$ hybrid was also confirmed by the smaller high-frequency semicircle in the electrochemical impedance spectroscopy results (EIS, Fig. 5b).[57] The photoelectrochemical characterizations indicated the accelerated separation and migration of photoinduced charges in the CdS@$CoTiO_3$ hybrid, and thus a prominent activity for photodegrading pollutants. Additionally, an obvious inhibition of the recombination of photogenerated e^-/h^+ in the CdS@$CoTiO_3$ hybrids was indicated by the PL emission spectrum. Generally, a weaker PL intensity means a higher separation and transfer performance of photogenerated e^-/h^+ pairs.[17,58] As presented

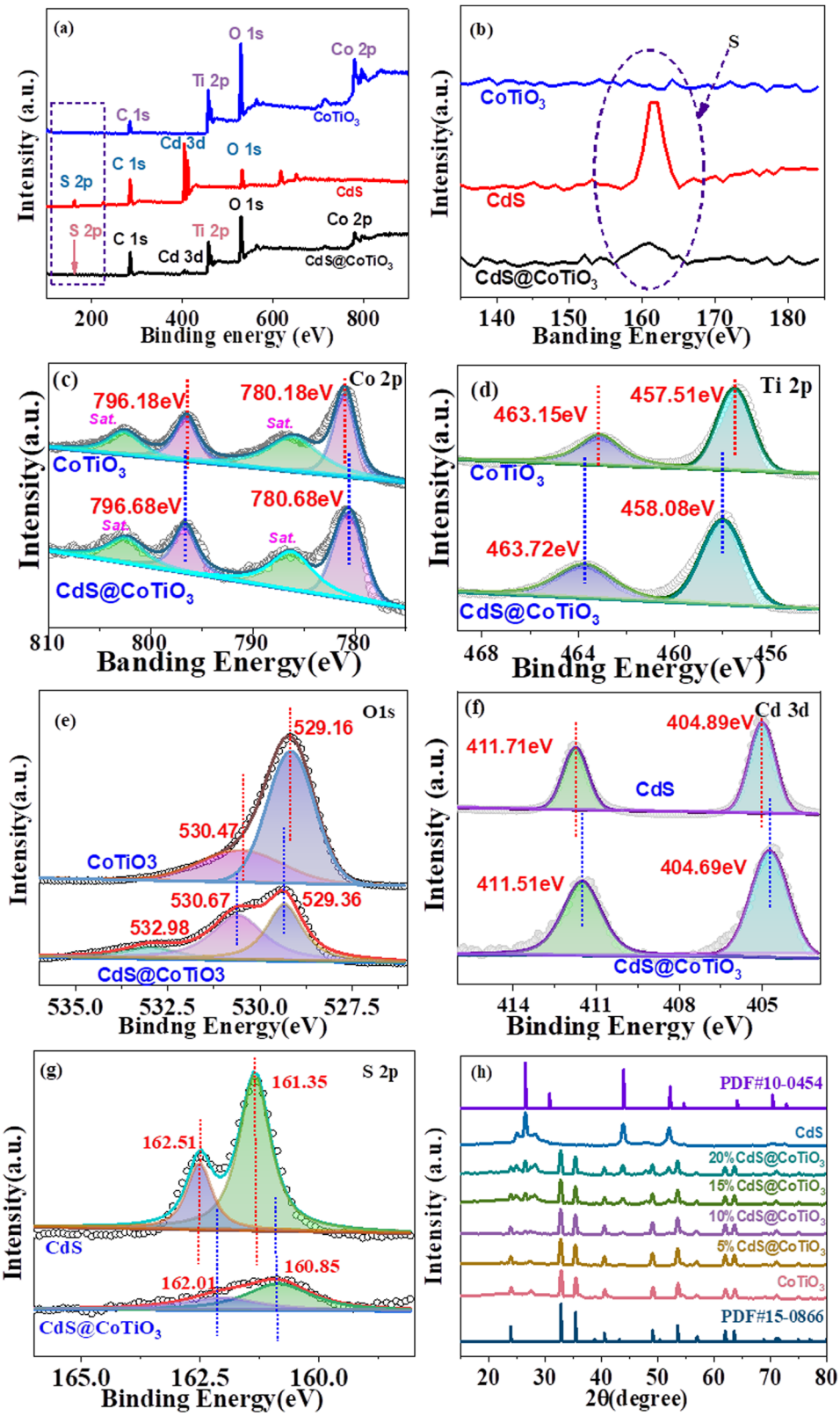

Fig. 3 (a) and (b) XPS survey spectra and high-resolution XPS spectra: (c) Co 2p, (d) Ti 2p, (e) O 1s, (f) Cd 3d, (g) S 2p; and (h) the XRD spectra of different samples.

in Fig. 5c, the emission intensity of the $CdS@CoTiO_3$ hybrids was remarkably weaker than those of CdS and $CoTiO_3$ alone, signifying the recombination of light-induced charges in the $CdS@CoTiO_3$ hybrids was effectively prohibited.

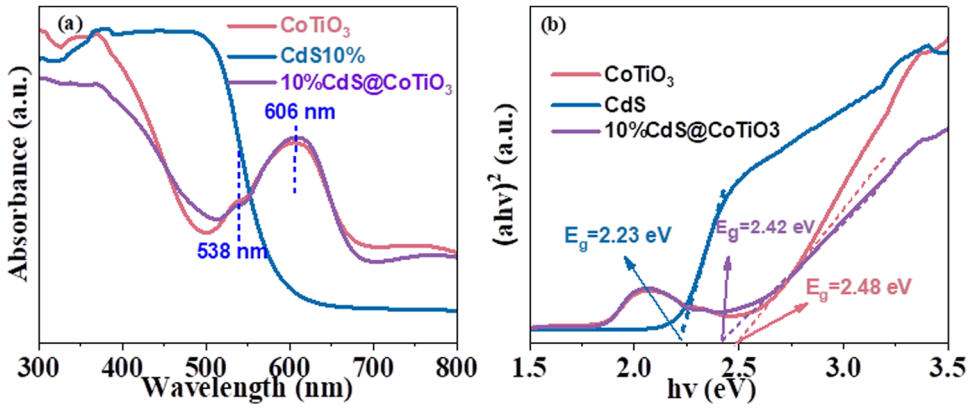

Fig. 4 (a) UV-vis-diffuse reflectance spectra and (b) corresponding $(\alpha h\nu)^2$ *versus* $h\nu$ curves of the pure $CoTiO_3$, CdS, and CdS@$CoTiO_3$ heterojunction.

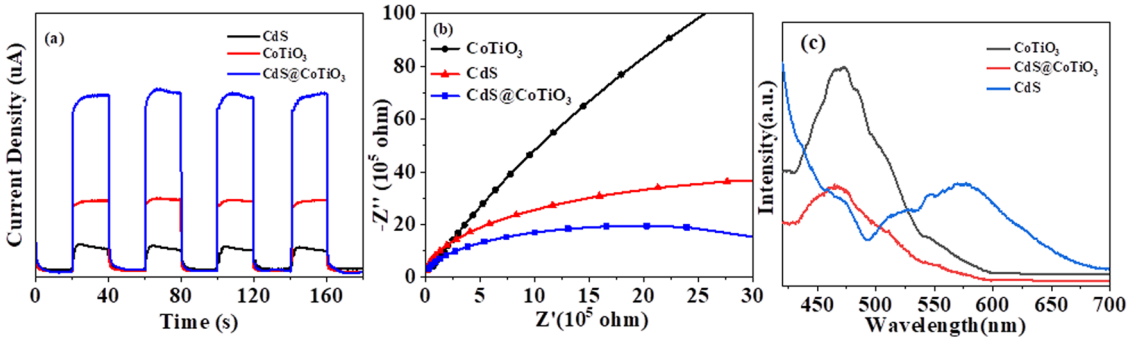

Fig. 5 (a) Visible-light photocurrent responses, (b) EIS Nyquist plots, and (c) PL plots of the pure $CoTiO_3$, CdS, and CdS@$CoTiO_3$ heterojunction.

To evaluate the photocatalytic activity of the as-prepared catalysts, the representative organic pollutant 2,4-DCP solution was chosen as a pollution model, as exhibited in Fig. 6. Clearly, all the samples were essentially saturated by adsorption within 40 min in the dark, with only a small decrease in the concentration of 2,4-DCP. Moreover, only a negligible removal of 2,4-DCP was observed in the absence of any photocatalyst, suggesting that 2,4-DCP exhibited excellent stability under visible-light irradiation (Fig. 6a). All the CdS@$CoTiO_3$ hybrids delivered boosted degradation capability toward 2,4-DCP compared with CdS and $CoTiO_3$ alone, which was attributed to the acceleration of the separation of photogenerated carriers and the strength of the redox capacity caused by the formation of a hollow core–shell Z-scheme heterojunction between CdS and $CoTiO_3$. Among the hybrids with different masses of CdS, 10% CdS@$CoTiO_3$ showed the highest activity, with a removal efficiency of approximately 91.3%, while 50% and 46% removal efficiencies were obtained for CdS and $CoTiO_3$ after 120 min visible irradiation. Fig. 6b displays the fitting of the kinetics of the photocatalytic degradation, whereby all the catalysts conformed to the quasi-first-order kinetic model. The kinetic constant (k) of 10% CdS@$CoTiO_3$ (0.018 min^{-1}) was about

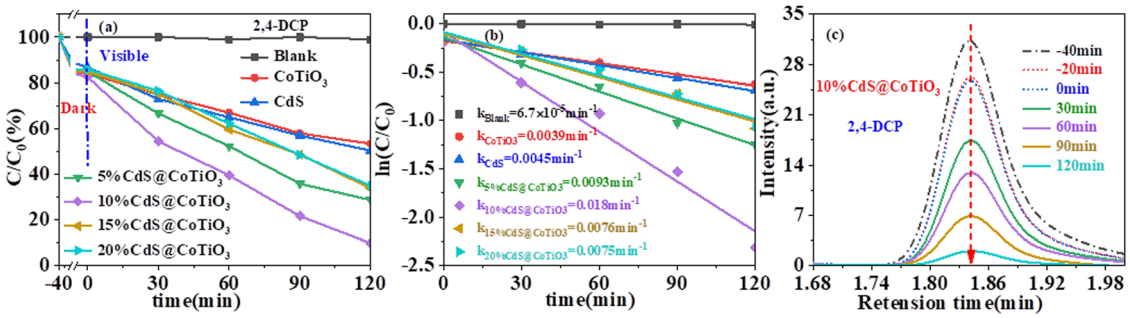

Fig. 6 (a) Photocatalytic degradation of 2,4-DCP aqueous solutions, and the (b) corresponding kinetic fitting curves over different samples under visible-light irradiation; and (c) corresponding UPLC plots of 2,4-DCP during degradation over the 10%CdS@$CoTiO_3$ hybrid.

4.0- and 4.6-times higher than those of pure CdS (0.0045 min^{-1}) and $CoTiO_3$ (0.0039 min^{-1}), respectively. The concentration changes of 2,4-DCP was detected by UPLC. As depicted in Fig. 6c, the intensity of the peak for 2,4-DCP rapidly decreased with increasing the irradiation time, suggesting that 2,4-DCP was gradually decomposed over the 10% CdS@$CoTiO_3$ heterojunction. Considering its most effective performance, 10% CdS@$CoTiO_3$ was chosen for the subsequent research studies, without special instructions.

Subsequently, the photocatalytic degradation of a well-known antibiotic (TC) was investigated to confirm the enhancement of the photodegradation performance of the 10% CdS@$CoTiO_3$ hybrids under identical conditions (Fig. 7). Obviously, the removal over the CdS@$CoTiO_3$ hybrids ($\approx$ 91.8%) was much higher than that for $CoTiO_3$ alone ($\approx$ 65.3%) with 80 min visible irradiation (Fig. 7a and b), with a k of 0.025 min^{-1}, which was 2.5-times higher than that of $CoTiO_3$ (0.010 min^{-1}). Furthermore, the photocatalytic degradation of TC was confirmed by recording its UV-visible spectral behavior at λ_{max} = 358 nm (Fig. 7c and d).

Generally, cycling stability is a crucial parameter to assess the industrialization potential of photocatalysts. Therefore, the 10% CdS@$CoTiO_3$ hybrid with the best catalytic activity was selected for the cycling tests, as shown in Fig. 8. It could be clearly seen that the photocatalytic performance was not significantly attenuated for 2,4-DCP degradation after four cycling tests (Fig. 8a). Furthermore, the XRD spectrum of 10% CdS@$CoTiO_3$ showed no obvious change after the reaction compared with that before, while the architectural structure of the CdS@$CoTiO_3$ hybrids was also well maintained after the cycles (Fig. 8b and c), further implying the satisfactory reusability and stability of CdS@$CoTiO_3$during the photocatalytic reaction.

Next, trapping tests were performed to investigate the reactive species taking part in the photodegradation of 2,4-DCP process. Experimentally, isopropanol (IPA), sodium oxalate ($Na_2C_2O_4$), and benzoquinone (BQ) were used to scavenge hydroxyl radicals ($^{\bullet}OH$), superoxide radicals ($^{\bullet}O_2^-$), and holes (h^+), respectively.[11] As illustrated in Fig. 9a, with the addition of IPA and BQ, the degradation efficiency of 2,4-DCP significantly decreased from 91.0% to 49.5% and 45.1%, indicating that $^{\bullet}OH$ and $^{\bullet}O_2^-$ as primary active species participated in 2,4-DCP degradation. Meanwhile, the remove efficiency was also inhibited from 91.0% to 61.9% after introducing $Na_2C_2O_4$, implying that h^+ also play a certain role in the photocatalytic degradation of 2,4-DCP. Furthermore, the generation of $^{\bullet}OH$ and $^{\bullet}O_2^-$ in the photocatalytic reaction system was further confirmed by EPR using DMPO as a free radical trapping agent, as exhibited in Fig. 9b. Clearly, no EPR signal was observed under the dark condition, indicating no $^{\bullet}OH$ or $^{\bullet}O_2^-$ were produced.[59,60] However, four characteristic signals of DMPO-$^{\bullet}OH$ possessing the intensity ratio of 1:2:2:1 were observed in the EPR spectrum after 5 min of visible-light irradiation. Similarly, typical DMPO-$^{\bullet}O_2^-$ adducts (quartet signal relative intensities

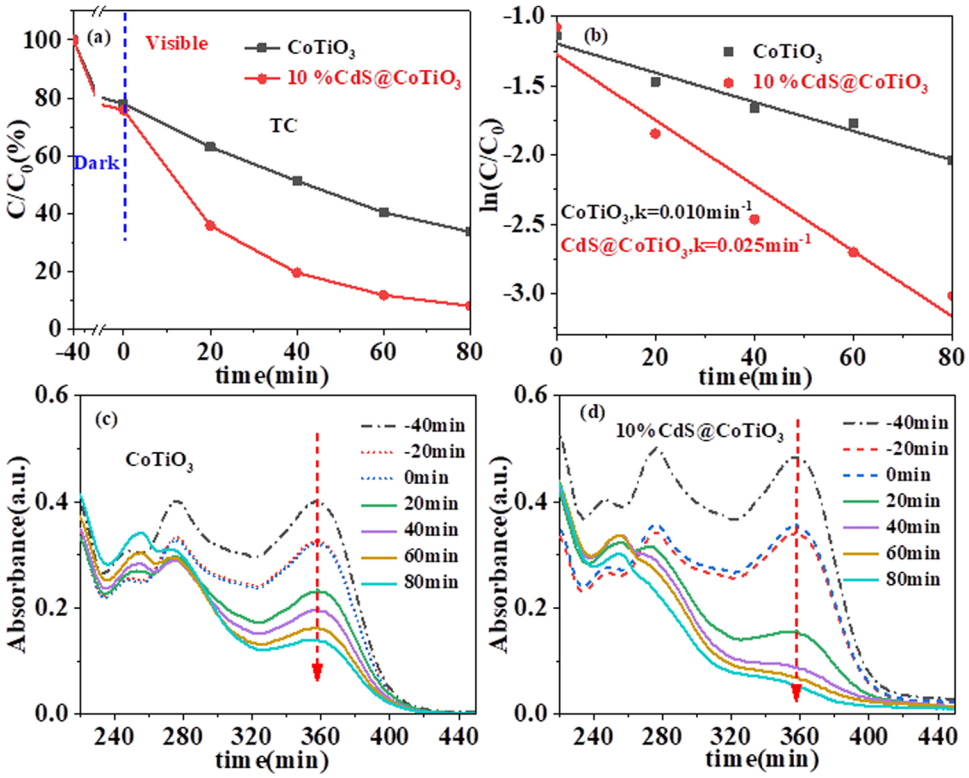

Fig. 7 (a) Photocatalytic degradation of TC aqueous solutions, and the (b) corresponding kinetic fitting curves over pure $CoTiO_3$ and (d) 10% CdS@$CoTiO_3$; time-dependent absorption spectra of TC degradation: (c) pure $CoTiO_3$, (d) 10% CdS@$CoTiO_3$.

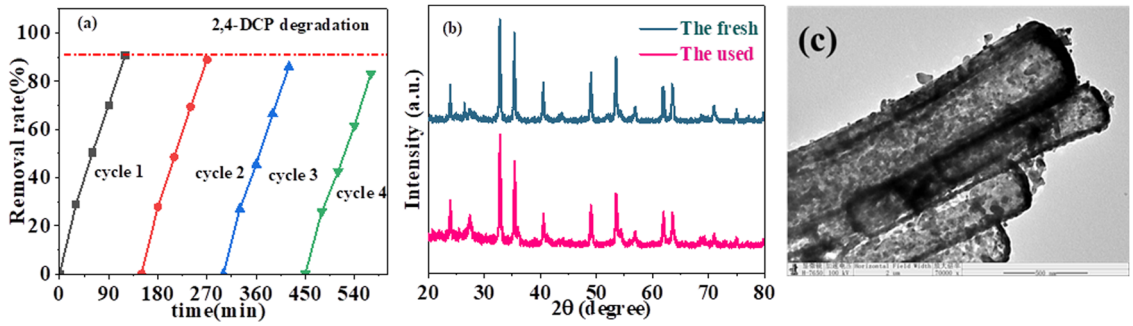

Fig. 8 (a) Reusability of the catalyst for the removal of 2,4-DCP under visible-light irradiation, (b) XRD patterns before and after the photocatalytic tests, and (c) TEM image of the CdS@$CoTiO_3$ hybrid after use.

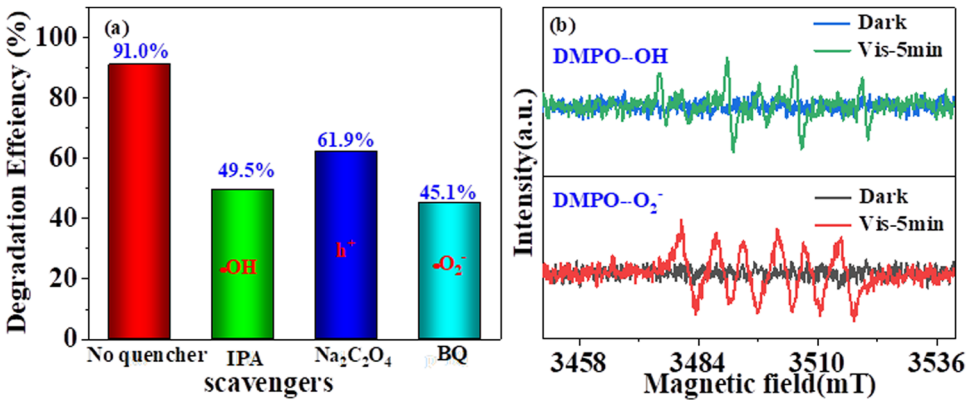

Fig. 9 (a) Influence of various scavengers on the degradation of 2,4-DCP and (b) EPR spectra in the dark and under visible-light irradiation for DMPO-•OH and DMPO-$•O_2^-$.

of 1 : 1 : 1 : 1) were also detected in the CdS@$CoTiO_3$ photocatalytic degradation system, illustrating the formation of $•O_2^-$. The EPR results unambiguously suggested that •OH and $•O_2^-$ radicals were both formed over the CdS@$CoTiO_3$ hybrids, which was well consistent with the active species trapping experimental results.

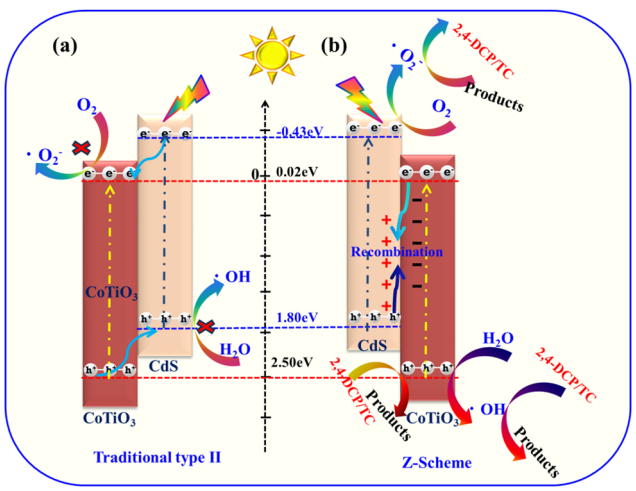

Scheme 2 Illustration of the photocatalytic degradation mechanisms for 3D CdS@$CoTiO_3$ heterojunctions: (a) type II and (b) Z-scheme.

Based on the energy band positions of CdS and $CoTiO_3$, as well as the results from the radical trapping tests and EPR analysis, a typical Z-scheme mechanism over the core–shell structured CdS@$CoTiO_3$ is proposed, as shown in Scheme 2. In this mechanism, owing to the narrow band gaps, both CdS and $CoTiO_3$ can be excited by visible light to generate electrons (e^-) in the conduction band (CB) and positive holes (h^+) in the valence band (VB) simultaneously. Generally, e^- transfer occurs from the $E_{C,CdS}$ to the $E_{C,CoTiO_3}$, meanwhile h^+ accumulate at $E_{V,CdS}$ (Scheme 2a, type-II heterojunctions). In such a case of charge-transfer behavior, the $E_{V,CdS}$ is not sufficient to oxidize OH^- ($E_{OH^-/•OH}$ = 2.38 eV *vs.* NHE) and the $E_{C,CoTiO_3}$ is unable to reduce O_2 to generate $•O_2^-$ ($E_{O_2/•O_2^-}$ = 0.33 eV *vs.* NHE).[61,62] Clearly, this is not consistent with the results of the trapping experiments, where $•O_2^-$ and •OH were found to be the major active species in the photocatalytic degradation 2,4-DCP system. For the Z-scheme mechanism, the photoinduced e^- in the CB of $CoTiO_3$ can transfer to the VB of CdS and recombine with the photogenerated h^+, which not only inhibits the self-recombination of e^-/h^+ pairs in both CdS and $CoTiO_3$ but also preserves the more negative CB potential of CdS and a more positive VB potential of $CoTiO_3$ for the photocatalytic reaction, thereby resulting in an efficient 2,4-DCP mineralization reaction. Drawing from the above analysis, the possible reaction equations could be elucidated as follows in eqn (4)–(7):

$$CdS@CoTiO_3 + h\nu \rightarrow CdS@CoTiO_3(h^+ + e^-) \quad (4)$$

$$CdS(e^-) + O_2 \rightarrow {}^{\bullet}O_2^- \quad (5)$$

$$CoTiO_3(h^+) + H_2O \rightarrow {}^{\bullet}OH + H^+ \quad (6)$$

$$2,4\text{-DCP/TC} + h^+/{}^{\bullet}O_2^-/{}^{\bullet}OH \rightarrow CO_2 + H_2O. \quad (7)$$

From the architectural point of view, the hierarchical hollow core–shell nature of the CdS@$CoTiO_3$ photocatalyst with large internal cavities indeed endow it with sufficient active sites, while also shortening the transport distance of photoinduced charges as well as improving the capture capacity for visible light, simultaneously.

4. Conclusions

In summary, a hierarchical core–shell CdS@$CoTiO_3$ photocatalyst was constructed by uniformly modifying a CdS NPs layer on the surface of $CoTiO_3$ hollow NRs. The experimental investigation and EPR analytical results confirmed the existence of a Z-scheme photoinduced carrier transport path between CdS and $CoTiO_3$. The Z-scheme heterojunction configuration combining this delicate architecture greatly decreased the recombination of photogenerated e^-/h^+ pairs while still retaining a strong oxidation and reduction ability, resulting in a dramatically improved photocatalytic degradation activity for 2,4-DCP and TC. Additionally, the hollow core–shell nanorod structure could maintain good photocatalytic stability. It is speculated that the strategy adopted in this work could also be expanded to other hollow $CoTiO_3$-based materials for applications not only in photocatalysis but also in other fields, such as energy storage and conversion, and electrochemistry.

Conflicts of interest

There are no conflicts to declare.

Acknowledgements

This project was supported by the National Natural Science Foundation of China (NSFC21906088) and (NSFC52170039), Heilongjiang Youth Innovative Talents Training Program for Universities (UNPYSCT-2020071). The authors also thank their colleagues and other students who participated in this study.

References

1 C.-C. Wang, J.-R. Li, X.-L. Lv, Y.-Q. Zhang and G. Guo, Photocatalytic organic pollutants degradation in metal–organic frameworks, *Energy Environ. Sci.*, 2014, **7**, 2831–2867.
2 D. Chen, Y. Cheng, N. Zhou, P. Chen, Y. Wang, K. Li, S. Huo, P. Cheng, P. Peng, R. Zhang, L. Wang, H. Liu, Y. Liu and R. Ruan, Photocatalytic degradation of organic pollutants using TiO_2-based photocatalysts: A review, *J. Cleaner Prod.*, 2020, **268**, 121725.
3 Y. Cheng, Y. Zhang, Z. Wang, R. Guo, J. You and H. Zhang, Review of Bi-based catalysts in piezocatalytic, photocatalytic and piezo-photocatalytic degradation of organic pollutants, *Nanoscale*, 2023, **15**, 18571–18580.
4 V. Gadore, S. R. Mishra and M. Ahmaruzzaman, Metal sulphides and their heterojunctions for photocatalytic degradation of organic dyes-A comprehensive review, *Environ. Sci. Pollut. Res.*, 2023, **30**, 90410–90457.
5 A. A. Okab, Z. H. Jabbar, B. H. Graimed, A. I. Alwared, S. H. Ammar and M. A. Hussein, A comprehensive review highlights the photocatalytic heterojunctions and their superiority in the photo-destruction of organic pollutants in industrial wastewater, *Inorg. Chem. Commun.*, 2023, **158**, 111503.
6 J. Low, J. Yu, M. Jaroniec, S. Wageh and A. A. Al-Ghamdi, Heterojunction Photocatalysts, *Adv. Mater.*, 2017, **29**, 1601694.
7 S. Cheng, Z. Sun, K. H. Lim, A. A. Wibowo, T. Zhang, T. Du, L. Liu, H. T. Nguyen, G. K. Li, Z. Yin and S. Kawi, Dual-Defective Two-Dimensional/Two-Dimensional Z-Scheme Heterojunctions for CO_2 Reduction, *ACS Catal.*, 2023, **13**, 7221–7229.
8 L. X. Wang, C. B. Bie and J. G. Yu, Challenges of Z-scheme photocatalytic mechanisms, *Trends Chem.*, 2022, **4**, 973–983.
9 J. Yu, C. Zhang, Y. Yang, T. Su, G. Yi and X. Zhang, 3D chrysanthemum-like g-C_3N_4/TiO_2 as an efficient visible-light-driven Z-scheme hybrid photocatalyst for tetracycline degradation, *Phys. Chem. Chem. Phys.*, 2023, **25**, 3848–3858.
10 F. Xing, C. Wang, S. Liu, S. Jin, H. Jin and J. Li, Interfacial Chemical Bond Engineering in a Direct Z-Scheme g-C_3N_4/MoS_2 Heterojunction, *ACS Appl. Mater. Interfaces*, 2023, **15**, 11731–11740.
11 F. Wang, T. Lu, X. Cheng, Y. Zhang and X. Xiao, Fabrication of $MoSe_2$/Bi_3O_4Br Z-scheme heterojunction with enhanced photocatalytic performance, *J. Environ. Chem. Eng.*, 2024, **12**, 111991.
12 H. Wang, Q. Liu, T. Ji, R. Zhao, L. Li, J. Han and L. Wang, Preparation of $Mn_{0.8}Cd_{0.2}S$/$NiCo_2S_4$ Z-scheme heterojunction composite for enhanced photocatalytic hydrogen production, *Surf. Interfaces*, 2024, **45**, 103900.
13 W. Wang, Z. Liu, H. Nie and B. Kong, The direct Z-scheme character and roles of S vacancy in BiOCl/Bi_2S_3-(001) heterostructures for superior photocatalytic activity: a hybrid density functional investigation, *Phys. Chem. Chem. Phys.*, 2024, **26**, 10723–10736.
14 S. Wang, B. Y. Guan and X. W. D. Lou, Construction of $ZnIn_2S_4$–In_2O_3 Hierarchical Tubular Heterostructures for Efficient CO_2 Photoreduction, *J. Am. Chem. Soc.*, 2018, **140**, 5037–5040.
15 D. Zheng, X.-N. Cao and X. Wang, Precise Formation of a Hollow Carbon Nitride Structure with a Janus Surface To Promote Water Splitting by Photoredox Catalysis, *Angew. Chem., Int. Ed.*, 2016, **55**, 11512–11516.
16 F. Zhao, Y. L. Law, N. Zhang, X. Wang, W. Wu, Z. Luo and Y. Wang, Constructing Spatially Separated Cage-Like Z-scheme Heterojunction Photocatalyst for Enhancing Photocatalytic H_2 Evolution, *Small*, 2023, **19**, 2208266.
17 C.-Q. Li, X. Du, S. Jiang, Y. Liu, Z.-L. Niu, Z.-Y. Liu, S.-S. Yi and X.-Z. Yue, Constructing Direct Z-Scheme Heterostructure by

Enwrapping $ZnIn_2S_4$ on CdS Hollow Cube for Efficient Photocatalytic H_2 Generation, *Adv. Sci.*, 2022, **9**, 2201773.

18 G.-Q. Zhao, X. Long, J. Zou, J. Hu and F.-P. Jiao, Design of hollow nanostructured photocatalysts for clean energy production, *Coord. Chem. Rev.*, 2023, **477**, 214953.

19 X. Li, J. Yu and M. Jaroniec, Hierarchical photocatalysts, *Chem. Soc. Rev.*, 2016, **45**, 2603–2636.

20 S. Wang, Y. Wang, S.-Q. Zang and X. W. Lou, Hierarchical Hollow Heterostructures for Photocatalytic CO_2 Reduction and Water Splitting, Small, *Methods*, 2020, **4**, 1900586.

21 X. Lin, Z. Xie, B. Su, M. Zheng, W. Dai, Y. Hou, Z. Ding, W. Lin, Y. Fang and S. Wang, Well-defined Co9S8 cages enable the separation of photoexcited charges to promote visible-light CO_2 reduction, *Nanoscale*, 2021, **13**, 18070–18076.

22 S. Wang, Y. Wang, S. L. Zhang, S.-Q. Zang and X. W. Lou, Supporting Ultrathin $ZnIn_2S_4$ Nanosheets on Co/N-Doped Graphitic Carbon Nanocages for Efficient Photocatalytic H_2 Generation, *Adv. Mater.*, 2019, **31**, 1903404.

23 X. Wang, C. Guo, X. Hu, Y. Xu, C. Zhang, J. Wei, J. Weng, Y. Liu, L. Fu, Q. Wang and T. Yang, Self-assembled oxygen vacancies modified hierarchical hollow tubular Bi_2WO_6/In_2O_3 Z-scheme heterojunction for optimized photocatalytic degradation of norfloxacin, *J. Environ. Chem. Eng.*, 2024, **12**, 112010.

24 S. Das, J. Pérez-Ramírez, J. Gong, N. Dewangan, K. Hidajat, B. C. Gates and S. Kawi, Core–shell structured catalysts for thermocatalytic, photocatalytic, and electrocatalytic conversion of CO_2, *Chem. Soc. Rev.*, 2020, **49**, 2937–3004.

25 J. Wang, R. Pan, S. Yan, R. Wang, X. Niu, Q. Hao, J. Ye, Y. Wu and H. Ying Yang, Construction of 1D/2D core-shell structured $K_6Nb_{10.8}O_{30}$@$Zn_2In_2S_5$ as S-scheme photocatalysts for cocatalyst-free hydrogen production, *Chem. Eng. J.*, 2023, **463**, 142489.

26 X. Li, H. Yang, Q. Peng, M. Zhu and J. Pan, CdS/$ZnSnO_3$ Hollow Core–Shell Nanocubes for Photocatalytic Hydrogen Evolution and Degradation of Ciprofloxacin, *ACS Appl. Nano Mater.*, 2024, **7**, 649–660.

27 X. Yang, S. Wei, X. Ma, Z. Gao, W. Huang, D. Wang, Z. Liu and J. Wang, Core–shell $CoTiO_3$@MnO_2 heterostructure for the photothermal degradation of tetracycline, *J. Mater. Sci.*, 2023, **58**, 3551–3567.

28 T. Li, X. Wang, Z. Jin and N. Tsubaki, Enhanced kinetics of photocatalytic hydrogen evolution by interfacial Co-C bonded strongly coupled S-scheme inorganic perovskite/organic graphdiyne (C_nH_{2n-2}) heterojunction, *Chem. Eng. J.*, 2023, **477**, 147018.

29 Y. Liu, J. Wu, X. Li, J. Chen, Y. Li, X. Luo, T. Xie, Q. Qiu and T. Liang, Highly efficient $CoTiO_3$/MOF-derived In_2S_3 photoelectrocatalysts: Degradation kinetics, pathways, and mechanism, *J. Alloys Compd.*, 2024, **975**, 172921.

30 B. Lin, S. Li, Y. Peng, Z. Chen and X. Wang, MOF-derived core/shell C-TiO_2/$CoTiO_3$ type II heterojunction for efficient photocatalytic removal of antibiotics, *J. Hazard. Mater.*, 2021, **406**, 124675.

31 R. Dadigala, R. Bandi, M. Alle, B. R. Gangapuram, V. Guttena and J.-C. Kim, In-situ fabrication of novel flower like MoS_2/$CoTiO_3$ nanorod heterostructures for the recyclable degradation of ciprofloxacin and bisphenol A under sunlight, *Chemosphere*, 2021, **281**, 130822.

32 L. Zheng, F. Teng, X. Ye, H. Zheng and X. Fang, Photo/Electrochemical Applications of Metal Sulfide/TiO_2 Heterostructures, *Adv. Energy Mater.*, 2020, **10**, 1902355.

33 X. Cong, A. Li, F. Guo, H. Qin, X. Zhang, W. Wang and W. Xu, Construction of CdS@g–C_3N_4 heterojunction photocatalyst for highly efficient degradation of gaseous toluene, *Sci. Total Environ*, 2024, **913**, 169777.

34 H. Ullah, Z. Haneef, A. Ahmad, I. S. Butler, R. N. Dara and Z. Rehman, MoS_2 and CdS photocatalysts for water decontamination: A review, *Inorg. Chem. Commun.*, 2023, **153**, 110775.

35 S.-R. Kim and W.-K. Jo, Application of a photostable silver-assisted Z-scheme $NiTiO_3$ nanorod/g-C_3N_4 nanocomposite for efficient hydrogen generation, *Int. J. Hydrogen Energy*, 2019, **44**, 801–808.

36 B. Su, H. Huang, Z. Ding, M. B. J. Roeffaers, S. Wang and J. Long, S-scheme $CoTiO_3$/$Cd_{9.51}Zn_{0.49}S_{10}$ heterostructures for visible-light driven photocatalytic CO_2 reduction, *J. Mater. Sci. Technol.*, 2022, **124**, 164–170.

37 S. Wang, B. Y. Guan, X. Wang and X. W. D. Lou, Formation of Hierarchical Co_9S_8@$ZnIn_2S_4$ Heterostructured Cages as an Efficient Photocatalyst for Hydrogen Evolution, *J. Am. Chem. Soc.*, 2018, **140**, 15145–15148.

38 R. Ye, H. Fang, Y.-Z. Zheng, N. Li, Y. Wang and X. Tao, Fabrication of $CoTiO_3$/g-C_3N_4 Hybrid Photocatalysts with Enhanced H_2 Evolution: Z-Scheme Photocatalytic Mechanism Insight, *ACS Appl. Mater. Interfaces*, 2016, **8**, 13879–13889.

39 T. Zhang, W. Wang, X. Jiang, H. Wang, Z.-H. He, Y. Yang, K. Wang, Z.-T. Liu and B. Han, Fabricating CdS/Ag/$BiVO_4$ Z-heterojunction for solvent-free photocatalytic oxidation of amines, *Green Chem.*, 2024, **26**, 3338–3345.

40 J. H. Wei, D. D. Han, J. T. Bi and J. B. Gong, Fe-doped ilmenite $CoTiO_3$ for antibiotic removal: Electronic modulation and enhanced activation of peroxymonosulfate, *Chem. Eng. J.*, 2021, **423**, 130165.

41 X. X. Lu, L. J. Wang, Q. Li, R. Luo, J. F. Zhang and Z. F. Tian, Construction of $CoTiO_3$/BiOI p-n heterojunction with nanosheets-on microrods structure for enhanced photocatalytic degradation of organic pollutions, *Adv. Powder Technol.*, 2022, **33**, 103354.

42 M. Mousavi and J. B. Ghasemi, Novel visible-light-responsive Black-TiO_2/$CoTiO_3$ Z-scheme heterojunction photocatalyst with efficient photocatalytic performance for the degradation of different organic dyes and tetracycline, *J. Taiwan Inst. Chem. Eng.*, 2021, **121**, 168–183.

43 Y. F. Jia, S. P. Li, H. Ma, J. Z. Gao, G. Q. Zhu, F. C. Zhang, J. Y. Park, S. Cha, J. S. Bae and C. Liu, Oxygen vacancy rich Bi_2O_4-Bi_4O_7-BiO_2 composites for UV-vis-NIR activated high efficient photocatalytic degradation of bisphenol A, *J. Hazard. Mater.*, 2020, **382**, 121121.

44 W. Jin, D. K. Liu, L. Y. Zhang, Q. Sun, Y. S. Wang, E. Z. Liu, X. Y. Hu and H. Miao, TiO_2 spatially confined growth of $Sb_2(S, Se)_3$@TiO_2 NT heterojunction photoanodes and their photoelectrochemical properties, *Catal. Sci. Technol.*, 2023, **13**, 7046–7058.

45 Z. R. Zhang, R. T. Guo, C. Xia, C. F. Li and W. G. Pan, B-TiO_2/$CuInS_2$ photocatalyst based on the synergistic effect of oxygen vacancy and Z-scheme heterojunction for improving photocatalyst CO_2 reduction, *Sep. Purif. Technol.*, 2023, **323**, 124416.

46 Z. Zhuang, Y. Li, Z. Li, F. Lv, Z. Lang, K. Zhao, L. Zhou, L. Moskaleva, S. Guo and L. Mai, MoB/g-C_3N_4 Interface Materials as a Schottky Catalyst to Boost Hydrogen Evolution, *Angew. Chem., Int. Ed.*, 2018, **57**, 496–500.

47 J. W. Fu, Q. L. Xu, J. X. Low, C. J. Jiang and J. G. Yu, Ultrathin 2D/2D WO_3/g-C_3N_4 step-scheme H_2-production photocatalyst, *Appl. Catal., B*, 2019, **243**, 556–565.

48 J. G. Yu, S. H. Wang, J. X. Low and W. Xiao, Enhanced photocatalytic performance of direct Z-scheme g-C_3N_4/TiO_2 photocatalysts for the decomposition of formaldehyde in air, *Phys. Chem. Chem. Phys.*, 2013, **15**, 16883–16890.

49 J. W. Fu, C. B. Bie, B. Cheng, C. J. Jiang and J. G. Yu, Hollow CoS_x Polyhedrons Act as High-Efficiency Cocatalyst for Enhancing the Photocatalytic Hydrogen Generation of g-C_3N_4, ACS Sustain, *Chem. Eng.*, 2018, **6**, 2767–2779.

50 H. Yang, X. Li, T. Zhao, Q. Peng, W. Yang, J. Cao, Y. Zheng, C. Li and J. Pan, The CdS/$CaTiO_3$ cubic core-shell composite towards enhanced photocatalytic hydrogen evolution and photodegradation, *Int. J. Hydrogen Energy*, 2023, **48**, 21788–21798.

51 A. Meng, S. Zhou, D. Wen, P. Han and Y. Su, g-C_3N_4/$CoTiO_3$ S-scheme heterojunction for enhanced visible light hydrogen production through photocatalytic pure water splitting, *Chin. J. Catal.*, 2022, **43**, 2548–2557.

52 K. Wangkawong, S. Suntalelat, D. Tantraviwat and B. Inceesungvorn, Novel $CoTiO_3$/Ag_3VO_4 Composite: Synthesis, Characterization and Visible-light-driven Photocatalytic Activity, *Mater. Lett.*, 2014, **133**, 119–122.

53 J. Zheng and L. Zhang, One-step in situ formation of 3D hollow sphere-like V_2O_5 incorporated $Ni_3V_2O_8$ hybrids with enhanced photocatalytic performance, *J. Hazard. Mater.*, 2021, **416**, 125934.

54 A. Meng, L. Zhang, B. Cheng and J. Yu, TiO_2–MnO_x–Pt Hybrid Multiheterojunction Film Photocatalyst with Enhanced Photocatalytic CO_2-Reduction Activity, *ACS Appl. Mater. Interfaces*, 2019, **11**, 5581–5589.

55 L. Chen, D. W. Meng, X. L. Wu, A. Q. Wang, J. X. Wang, Y. Q. Wang and M. H. Yu, In Situ Synthesis of V^{4+} and Ce^{3+} Self-Doped $BiVO_4$/CeO_2 Heterostructured Nanocomposites with High Surface Areas and Enhanced Visible-Light Photocatalytic Activity, *J. Phys. Chem. C*, 2016, **120**, 18548–18559.

56 J. Zhang, J. Ma, X. Sun, Z. Yi, T. Xian, X. Wu, G. Liu, X. Wang and H. Yang, Construction of Z-Scheme Ag_2MoO_4/$ZnWO_4$ Heterojunctions for Photocatalytically Removing Pollutants, *Langmuir*, 2023, **39**, 1159–1172.

57 Y. X. Geng, D. Y. Chen, N. J. Li, Q. F. Xu, H. Li, J. H. He and J. M. Lu, Z-scheme 2D/2D α-Fe_2O_3/g-C3N4 heterojunction for photocatalytic oxidation of nitric oxide, *Appl. Catal., B*, 2021, **280**, 119409.

58 L. Tang, C. Y. Feng, Y. C. Deng, G. M. Zeng, J. J. Wang, Y. N. Liu, H. P. Peng and J. J. Wang, Enhanced photocatalytic activity of ternary Ag/g-C_3N_4/$NaTaO_3$ photocatalysts under wide spectrum light radiation: The high potential band protection mechanism, *Appl. Catal., B*, 2018, **230**, 102–114.

59 H. J. Ding, L. P. Bao, Y. Su, Y. Q. Li, G. D. Xu, C. H. Dai and C. Zeng, Core-shell structured Z-scheme Ag_2S/$AgIO_3$ composites for photocatalytic organic pollutants degradation, *J. Environ. Manag.*, 2022, **313**, 115008.

60 W. J. Wang, Z. T. Zeng, G. M. Zeng, C. Zhang, R. Xiao, C. Y. Zhou, W. P. Xiong, Y. Yang, L. Lei, Y. Liu, D. L. Huang, M. Cheng, Y. Y. Yang, Y. K. Fu, H. Z. Luo and Y. Zhou, Sulfur doped carbon quantum dots loaded hollow tubular g-C_3N_4 as novel photocatalyst for destruction of Escherichia coli and tetracycline degradation under visible light, *Chem. Eng. J.*, 2019, **378**, 122132.

61 M. Chen, C. S. Guo, S. Hou, J. P. Lv, Y. Zhang, H. Zhang and J. Xu, A novel Z-scheme AgBr/P- g-C_3N_4 heterojunction photocatalyst: Excellent photocatalytic performance and photocatalytic mechanism for ephedrine degradation, *Appl. Catal., B*, 2020, **266**, 118614.

62 S. H. Cao, Y. Q. Zhao, J. Y. Guo, M. J. Fu, X. D. Yu, L. X. Ren, H. Chen and F. Jiang, Dual role of nickel acetylacetonate in visible light enhanced hydrogen production and antibiotics degradation of nickel/nickel oxides embedded-graphitic carbon nitrides, *Int. J. Hydrogen Energy*, 2024, **55**, 882–892.

